Nineteenth-century nanotechnology: The plasmonic properties of daguerreotypes

Andrea E. Schlather[a], Paul Gieri[b], Mike Robinson[c], Silvia A. Centeno[a], and Alejandro Manjavacas[b,1]

[a]Department of Scientific Research, The Metropolitan Museum of Art, New York, NY 10028; [b]Department of Physics and Astronomy, University of New Mexico, Albuquerque, NM 87131; and [c]Century Darkroom, Toronto, ON M4M 2S1, Canada

Edited by Catherine J. Murphy, University of Illinois at Urbana–Champaign, Urbana, IL, and approved May 2, 2019 (received for review March 12, 2019)

Plasmons, the collective oscillations of mobile electrons in metallic nanostructures, interact strongly with light and produce vivid colors, thus offering a new route to develop color printing technologies with improved durability and material simplicity compared with conventional pigments. Over the last decades, researchers in plasmonics have been devoted to manipulating the characteristics of metallic nanostructures to achieve unique and controlled optical effects. However, before plasmonic nanostructures became a science, they were an art. The invention of the daguerreotype was publicly announced in 1839 and is recognized as the earliest photographic technology that successfully captured an image from a camera, with resolution and clarity that remain impressive even by today's standards. Here, using a unique combination of daguerreotype artistry and expertise, experimental nanoscale surface analysis, and electromagnetic simulations, we perform a comprehensive analysis of the plasmonic properties of these early photographs, which can be recognized as an example of plasmonic color printing. Despite the large variability in size, morphology, and material composition of the nanostructures on the surface of a daguerreotype, we are able to identify and characterize the general mechanisms that give rise to the optical response of daguerreotypes. Therefore, our results provide valuable knowledge to develop preservation protocols and color printing technologies inspired by past ones.

daguerreotype | plasmon | color printing | metal nanoparticle | scattering

In today's digital age, photographic prints can seem like a relic from the past. For centuries, people searched for increasingly better ways to capture an image. Images projected by the camera obscura were used as guides for drawing and painting natural scenes and portraits at least from the 17th century (1, 2); however, these images could not be directly captured permanently. Inventors and early photographers understood that capturing an image would require an interaction of light and matter and identified different suitable photoreactive materials, silver halides among them, which quickly became the base of a sustained photographic technology that remains popular today in artistic photography (1, 3–5). Among the various early processes relying on the light sensitivity of silver halides, daguerreotypy was the first to become commercially successful and vastly popular (6, 7). The process was invented by Louis-Jacques-Mandé Daguerre (1787–1851) over several decades and, after much secret experimentation, it was presented to the French Academy of Sciences in Paris in 1839 (8, 9). The result was an image that, even by today's standards, had an extraordinary resolution and dynamic range (6, 7). Even though the process was quickly replaced by faster and less expensive methods, up to 3 million daguerreotypes were made every year in Europe and North America from 1839 to the 1860s (6, 10).

Two centuries later, there is much focus on engineering nanoscale light–matter interactions for improved color filters (11–14) and new color printing technologies (15–17). One promising approach utilizes metallic nanostructures (18–26), which possess electrons that can move freely and couple strongly to light, giving rise to collective oscillations known as surface plasmons (27, 28). Due to their strong interaction with light, plasmons supported by a metallic nanostructure determine its optical response. Furthermore, the nanostructure's morphology and material composition dictate the plasmon resonant frequency and hence which frequencies are absorbed and scattered when the nanostructure is illuminated (29). This, along with long-term durability, material simplicity, and subdiffraction limit spatial resolution, makes plasmonic nanostructures an ideal platform for color printing applications (30–32). Indeed, there is clear evidence that metal nanostructures have been used since ancient times to provide color to glass and pottery (33, 34).

Daguerreotypes, unlike other types of photographs, rely on light scattering by metallic nanoparticles to create an image that projects off a reflective silver substrate. The balance between the light scattered by the nanostructures and the specular reflection of the substrate creates the bright and dark tones, respectively, with the behavior of the midtones depending on the density of nanostructures, as can be seen in Fig. 1 *A* and *B* for a historical daguerreotype from the study collection of The Metropolitan Museum of Art. Quite uniquely, the image tones of a daguerreotype are also dynamic and can change significantly with the viewing angle. In this sense, daguerreotypes can be considered the first realization of plasmonic color printing. Indeed, novel proposals for the fabrication of these devices resemble daguerreotypy (35).

Daguerreotypes are irreplaceable records of history and culture that must be preserved for posterity, which requires an in-depth understanding of the physical and chemical mechanisms responsible for their optical response. To this date,

Significance

Daguerreotypes, among the earliest photographs of the 19th century, owe their incredible optical properties, image resolution, and dynamic range to light scattering produced by metallic nanostructures on their surface. Here we provide a detailed experimental and theoretical analysis on how the material composition, morphology, and dimensions of these nanostructures determine the characteristics of the daguerreotype image. Our results provide a scientific understanding of the unique optical effects of these artworks and therefore, in addition to providing valuable insight for developing preservation protocols, can inspire additional approaches for color printing, where nanostructures are directly manufactured by light.

Author contributions: A.E.S., S.A.C., and A.M. designed research; A.E.S., P.G., S.A.C., and A.M. performed research; M.R. contributed new reagents/analytic tools; A.E.S., P.G., M.R., S.A.C., and A.M. analyzed data; and A.E.S., P.G., M.R., S.A.C., and A.M. wrote the paper.

The authors declare no conflict of interest.

This article is a PNAS Direct Submission.

See Commentary on page 13724.

[1]To whom correspondence may be addressed. Email: manjavacas@unm.edu.

Published online June 10, 2019.

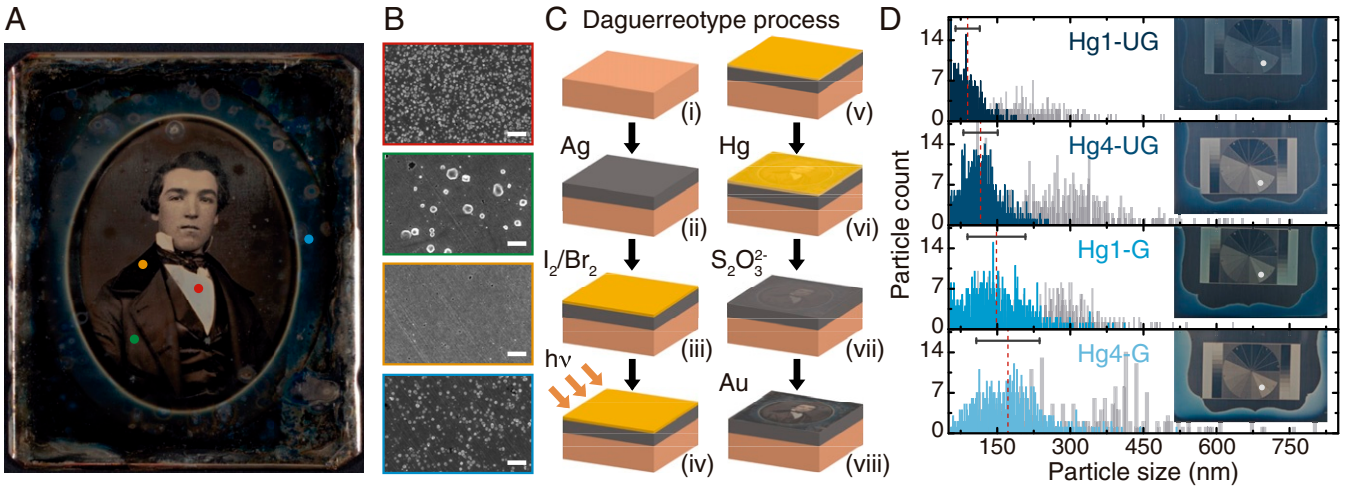

Fig. 1. Daguerreotype characteristics. (*A*) Daguerreotype in the study collection of The Metropolitan Museum of Art (artist unknown, ca. 1850s). The perimeter has a blue gradient created by an oval mask applied during sensitizing and mercury development. (*B*) Scanning electron microscope (SEM) images, outlined in colors corresponding to colored circles in *A*, show varying nanoparticle densities, from *Top* to *Bottom*, in highlight, midtone, shadow, and blue-tinted regions of the image. (Scale bars, 2 μm.) (*C*, *i–viii*) Schematic outlining the steps of the daguerreotype process. (*D*) Particle size counts, averages (red dashed line), and SD (black bar) for daguerreotype samples (*Insets*). Hg1 and Hg4 refer to minutes of mercury exposure, and UG and G refer to ungilded and gilded plates, respectively. Blue lines represent blue mask regions, while gray lines correspond to the regions of highest light exposure (i.e., highest particle density) of the exposure step wheels, marked by gray circles in *Insets*.

and compared with the number of daguerreotypes reported to have been produced in the 19th century, only a relatively small number of plates have been examined beyond conventional optical microscopy with spectroscopic techniques, scanning electron microscopy (SEM), and other nanoscale imaging methods capable of examining and characterizing the nanostructures on their surface (6, 36–47). Unfortunately, time and exposure to the elements have irreversibly altered 19th-century daguerreotype images, making it difficult to use them to characterize their properties. Also, it is rarely possible to remove microsamples for analysis from these unique objects. In this context, creating model daguerreotypes strictly following 19th-century practices becomes necessary, especially to recreate certain visual effects that have been observed in historical plates (42–44, 48).

In this article, we attempt to shine light on the daguerreotype's dimensionality using a unique combination of daguerreotype artistry and expertise, experimental nanoscale surface analysis, and electromagnetic simulations, to uncover the plasmonic properties of these early photographs. This combination provides a unique perspective into the mechanisms that give rise to their optical response, thus serving to inform the development of preservation protocols, as well as novel approaches to future color printing technologies inspired by past ones.

Results and Discussion

Soon after Daguerre's first manual was published, the daguerreotype process rapidly spread across England and North America (6, 48). Each of the numerous steps to make a daguerreotype demanded parametric control that strongly affected the appearance of the final image, of which a lack of mastery contributed to the failure of many early attempts (49–51). For a process that was as much a protocol as it was an art, diagnosing problems and obtaining desired results were accomplished by experimentation. The steps involved in making a daguerreotype are summarized in Fig. 1 *C* (for detailed information, see *Materials and Methods*). First, a silver (Ag) layer was joined to a copper plate by cladding and, in some instances, an additional layer of silver was deposited by electroplating (termed "galvanizing" in the 19th century) (Fig. 1 *C*, *i* and *ii*). The silver surface was polished and then sensitized with iodine fumes to create a photoactive silver iodine layer (Fig. 1 *C*, *iii*). With ever-changing parameters like temperature affecting their protocols, daguerreotypists relied on the observation of the color arising from reflection on the silver halide layer to estimate the readiness of the plate (48, 52). As the process improved, the ideal layer color evolved: Daguerre's first recommendation was golden yellow, with an average film thickness of 30 nm (52), but later changed it to "rose-violet," the color known after 1859 as magenta (48, 53). After 1840, further sensitization with bromides and chlorides followed, the additional halides creating trap states in the crystalline film that broadened its spectral sensitivity across the visible spectrum, thereby shortening light exposure times by up to a factor of 60. Exposure to light (Fig. 1 *C*, *iv*) catalyzed a photolytic reduction of the silver halides to create the latent image (Fig. 1 *C*, *v*), metallic silver clusters with diameters likely no more than 1–2 nm (54), which serve as nucleation sites for crystal growth by development with mercury (Hg) vapor. Mercury development took only a few minutes and resulted in fast formation of silver–mercury nanoparticles (Fig. 1 *C*, *vi*), via a complex combination of oxidation–reduction reactions, electrostatic processes, mass transfer of silver and mercury, and Ostwald ripening of metallic clusters (48, 55, 56). Afterward, the plate was placed in a bath of aqueous thiosulphate (Fig. 1 *C*, *vii*) to dissolve the unexposed silver halides and stop the light-sensitive reaction, a process known as "fixing." In a last step commonly referred to as "gilding," a gold salt solution was poured over the mercury-developed image and heated with a lamp. This created a nanoscale layer of gold (Au) on the surface, improving the visual contrast and, in principle, producing a more stable image (43, 44, 57).

The macroscale result is a unique and irreproducible positive image encoded in the nanoscale by metallic nanoparticles of myriad sizes, compositions, and surface densities. The Ag-Hg particle sizes are correlated with the density of latent image sites, which depends on the amount of light exposure on that area, as the concentration of mercury during development should remain relatively uniform across the exposure field (48). Thus, areas with lower nanoparticle density tend to have larger, more mercury-rich particles spaced farther apart, while high-density areas have smaller, silver-rich nanoparticles (6, 36, 41–43, 45, 48). The daguerreotype's optical response results from the collective light scattering produced by the ensemble of nanoparticles.

Through experimentation, daguerreotypists understood that certain conditions resulted in distinct optical effects that today are known to be the result of controlling nanoparticle size and homogeneity. Almost 100 years before the advent of color photography, overexposed skies depicted in daguerreotypes often appeared blue, an effect known in the Daguerreian era as "solarization." A common nuisance in photography, daylight skies are often overexposed to properly expose the subject. While overexposure creates white saturation on film or a digital detector, it creates a blue tint on a daguerreotype. The increased number of nucleation sites competing for mercury during the development stage produces particles with smaller average diameters and a narrower size distribution than nonsolarized areas, as demonstrated with the model daguerreotype samples in Fig. 1*D*. The inner region of each sample contains an exposure step wheel ranging from shadows to highlights and a solarized outer border, which appears blue at normal incidence. In these samples, two experimental conditions determine the varying shade of blue and the appearance and tone of the step wheel: the Hg development time, being either 1 min (Hg1) or 4 min (Hg4), and the absence or presence of gilding, referred to as ungilded (UG) or gilded (G), respectively. Analysis of particle diameter and height using atomic force microscopy (AFM), shown in Fig. 1*D*, confirms that longer Hg development times lead to larger overall particle diameters, as well as larger size deviations from the average particle diameter. The Au layer from the final gilding step also increases the overall average particle diameter and size distribution.

To understand how the properties of an ungilded daguerreotype image are determined by the nanoparticles on its surface, we investigated the optical response of a representative individual nanostructure chosen based on information obtained from high-angle scanning electron microscopy (HA-SEM) (Fig. 2*A*). We modeled it as an axially symmetric ellipsoid with dimensions d and h, which is half-embedded in the substrate, as shown in the schematics in Fig. 2*B*. The material of the nanoparticle was taken as a 70% silver–30% mercury alloy, in accordance with SEM-coupled energy dispersive spectroscopy (SEM-EDS) measurements (47, 48), while the substrate was assumed to be pure silver. Fig. 2*C* shows the scattering intensity for a particle with $d = 116$ nm and $h = 98$ nm, corresponding to the average particle size from the Hg4-UG solarized sample, calculated by solving numerically Maxwell's equations (*Materials and Methods*). The blue and red curves indicate, respectively, the results for illumination with S or P polarized light (Fig. 2*B*), while the black line corresponds to their average, representing illumination with unpolarized light. In all cases, the angle of incidence is 45°. The spectrum is dominated by two different modes: a narrow peak in the blue/UV part of the spectrum (≈365 nm) and a broader one in the red part of the spectrum (≈670 nm). These two modes are associated, respectively, with dipoles that oscillate parallel and perpendicularly to the substrate, as confirmed by the charge plots shown in Fig. 2 *D* and *F*. Consequently, the first mode radiates mostly in the vertical direction, as seen in Fig. 2*E*, while the second one radiates at high angles with respect to the vertical direction, with the doughnut-shaped pattern shown in Fig. 2*G*. The large difference in the radiation patterns of these modes has direct consequences on the angle dependence of the daguerreotype response. Specifically, when observed at small angles with respect to the vertical, we expect its response to be dominated by the mode located in the blue/UV, while, at large angles, the response is dominated by the mode on the red end of the spectrum. Therefore, as the viewing angle increases, the color of the daguerreotype is expected to evolve from a blue hue to a red one.

This is confirmed by the scattering intensity spectra plotted in Fig. 3*A*, calculated for particles with sizes corresponding to the average dimensions of the solarized regions of the Hg1-UG

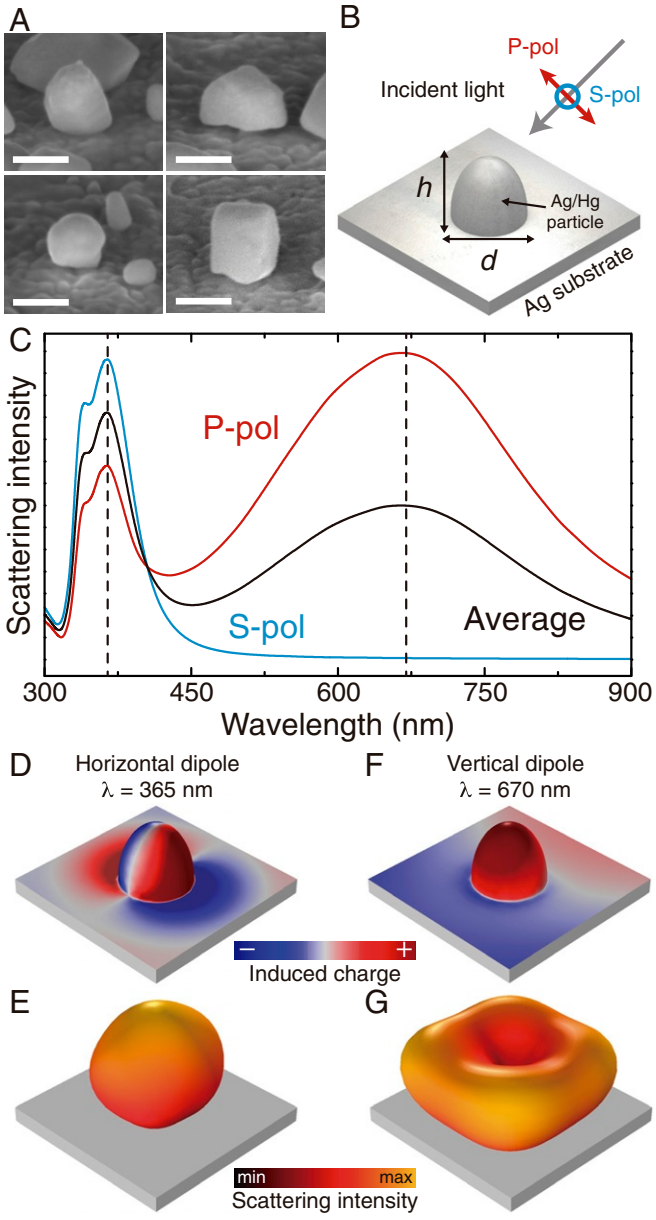

Fig. 2. Analysis of the optical response of an individual nanostructure. (*A*) High-angle scanning electron microscope (HA-SEM) image of nanostructures on the daguerreotype surface. (Scale bar, 200 nm.) (*B*) Schematic diagram of the simulation geometry. (*C*) Calculated scattering spectra for a nanostructure with $h = 98$ nm and $d = 116$ nm. The blue and red curves show, respectively, the results for illumination with S or P polarization (*B*), while the black curve corresponds to averaged results. (*D*–*G*) Induced charge (*D* and *F*) and radiation pattern (*E* and *G*) for the horizontal and vertical dipole modes, calculated at 365 nm and 670 nm, respectively.

(solid curves) and Hg4-UG (dashed curves) samples, at four different viewing angles with respect to the vertical direction: 0°, 30°, 60°, and 80°. As expected, for 0°, the optical response is entirely located in the blue/UV part of the spectrum. Then, as the angle increases, the scattering spectrum begins to display a second peak at longer wavelengths, which, for 80°, completely dominates the spectra. This effect explains why this daguerreotype, when viewed from above, exhibits a blue tone, while, for increasing view angles, the tone shifts to a brown/red, as can be seen from the angled microscope images of the surfaces of the Hg1-UG (Fig. 3*B*) and the Hg4-UG (Fig. 3*C*) daguerreotype samples. It is important to note that, although the angle

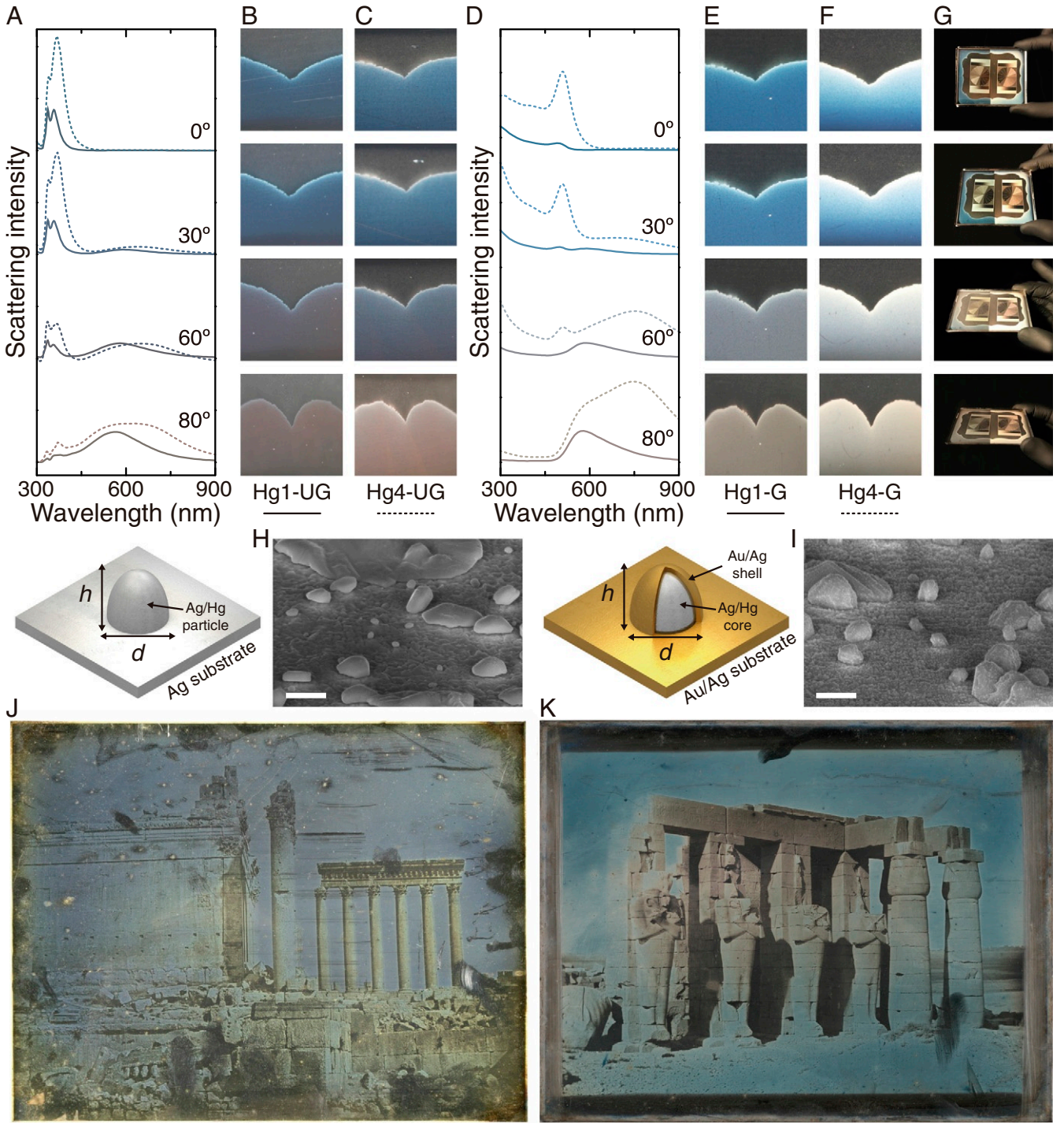

Fig. 3. Viewing angle dependence of the daguerreotype image. (*A*) Calculated scattering intensities for 0°, 30°, 60°, and 80° viewing angles for the Hg1-UG (solid curves) and Hg4-UG (dashed curves) samples. (*B* and *C*) Microscope images of the surface of the Hg1-UG and Hg4-UG samples taken at the angles shown in *A*. (*D–F*) Same as *A–C*, but for gilded samples. (*G*) Photographs of the entire Hg1/4-G sample taken at different angles. The left part of the plate corresponds to the Hg1-G sample, while the Hg4-G sample is located on the right. (*H* and *I*) HA-SEM images of the structures in model ungilded and gilded daguerreotype samples, respectively. (Scale bars, 500 nm.) The schematics at *Left* of the SEM images describe the geometry used to model the response of the nanostructures. (*J*) *Baalbec, 1844. Petit et Grand Temple*, Girault de Prangey, Bibliothèque Nationale de France (ark:/12148/btv1b6903484v). Source: gallica.bnf.fr/National Library of France. (*K*) *Ramesseum, Thebes, 1844*. Girault de Prangey, The Metropolitan Museum of Art (2016.604).

dependence results from the different nature of the modes supported by the nanoparticles, their wavelengths, as well as the scattering intensity, depend on the actual size of the nanoparticle. Indeed, examining Fig. 3 *A–C*, we observe that the Hg4-UG sample, which has larger average particle sizes, displays larger and broader peaks, as well as an overall redshift, compared with the Hg1-UG sample.

The variation of color hue with viewing angle also occurs for gilded daguerreotypes, as shown in Fig. 3 *D–F*. These samples, as discussed above, underwent an extra step in which a

thin gold/silver film was created on their surface. We modeled them by adding a shell made of a 90% gold–10% silver alloy, which coats the silver–mercury particle (44, 47), as shown in the schematics below Fig. 3 *A* and *D*. The thickness of this shell was taken from the difference of the average diameters measured for the gilded and ungilded samples. In addition to the shell layer, the substrate for the gilded samples was also modeled using the same gold–silver alloy instead of pure silver. This model was used for the angle-dependent scattering calculations shown in Fig. 3*D*. The solid and dashed curves correspond, respectively, to the Hg1-G and the Hg4-G samples. The results of our modeling show that the gilding process leads to an overall redshift of the spectra, as expected from the smaller plasma frequency and interband transition threshold of gold compared with silver, but it does not alter the angle dependence discussed previously for the ungilded samples. The spectra still contain two modes: one at lower wavelengths, in this case near 500 nm, which primarily radiates in the vertical direction, and another at larger wavelengths, which radiates at high angles. This clearly explains the angle-dependent color hue of the gilded daguerreotypes seen in Fig. 3 *E* and *F*, as well as in Fig. 3*G*, which displays photographs of the entire Hg1/4-G daguerreotype plate taken at the different viewing angles.

Daguerreotypes were gilded to give images greater contrast, as well as a desirable warmer tone. Nineteenth-century daguerreotypists assumed the gold layer also protected the images against damage. Comparison between the particles in the high-density regions of ungilded and gilded samples using HA-SEM (Fig. 3 *H* and *I*) shows an increase in surface roughness and average image particle size in the gilded samples. Fig. 3 *J* and *K* shows examples of an ungilded and a gilded historical daguerreotype, both created in 1844 by French daguerreotypist Joseph-Philibert Girault de Prangey (1804–1892). During his travels throughout Europe and the Middle East in the early 1840s, de Prangey created over 1,000 daguerreotypes. His work comprises some of the first recorded photographs of cultural monuments and historical sites. While the majority of these plates were gilded, many were left ungilded, and the distinct visual appearances can be readily apparent (58). Although conditions of plate creation, storage, and treatment histories are not known, a few characteristics are clear; while both plates show solarization, the tone of the solarized regions in the ungilded plate is a gray-blue, whereas the gilded daguerreotype solarized regions have a blue-green tone, along with a higher contrast between shadows and highlights. This is consistent with the redshift of the scattering peaks caused by the gold layer described above. Furthermore, ungilded image particles can be easily removed with the swipe of a finger while, in gilded plates, the image particles are surrounded with a nanoscale layer of gold (43), effectively "gluing" them to the mirror surface.

The surface of a daguerreotype can contain a broad range of particles sizes and morphologies, with no two daguerreotypes being the same. This range is highlighted by the HA-SEM images shown in Fig. 3 *H* and *I*, as well as the histograms in Fig. 1*D*. So far, we have modeled the response of the different samples using the simplest morphology, a hemisphere, with dimensions matching averaged values obtained in the measurements, and assumed the particles to be made of a 70% silver–30% mercury alloy. However, the optical response of any daguerreotype results from a collective response of many particles, so it is important to understand how the variation of the different parameters, including size, shape, and composition, impacts the scattering spectrum of the particle. In Fig. 4*A*, we investigated the effect of material composition by calculating the scattering intensity of particles with $d = 116$ nm and $h = 98$ nm, made of silver–mercury alloys with different ratios, as indicated in the legend. As the silver content grows, and consequently the mercury content decreases, the two peaks in the scattering spectrum increase in height and become narrower. This is explained by the smaller absorption losses of silver, compared with mercury, in the range of wavelengths under study, as can be seen by examining the imaginary part of their dielectric functions (Fig. 4*A*, *Left Inset*). Importantly, despite these changes, the overall behavior of the scattering spectrum remains almost unchanged. The effect of the morphology is studied in Fig. 4*B* through the analysis of the response of particles with different heights, h, but constant diameter, $d = 116$ nm. The variation of h affects primarily the vertical dipole mode: As it is reduced, this mode blueshifts and eventually merges with the horizontal dipole mode. At the same time, the intensity of the whole scattering spectrum, which is proportional to the volume of the particle (59), is reduced.

A key geometric characteristic that gives this system its unique features is the conductive contact between the particle and the substrate. In Fig. 4*C*, we analyzed the effect of changing the contact area by modeling particles with $d = 116$ nm and $h = 98$ nm and different levels of penetration into the substrate, s, as shown in Fig. 4*C*, *Inset*. We observed that, as s increases, i.e., as the particle moves out of the surface, both peaks in the scattering spectrum redshift. This can be attributed to the increase in volume, which also produces a broadening of the peaks due to the increase of the radiative losses (59). As expected, these effects are more pronounced for the vertical dipole mode, since, due to its nature, its optical properties depend directly on the total height and the contact area. The final aspect we analyzed was the effect of the overall dimensions of the nanoparticle. Fig. 4*D* shows the scattering intensity for particles with different d and h, as indicated in Fig. 4*D*, *Inset*. The results are consistent with the previous analysis: As the dimensions of the nanoparticle increase, the scattering spectra experience an overall redshift and the peaks become broader.

We conclude that, while the particle composition does not significantly alter the response of the nanoparticle, its morphology and size do have a strong impact on the scattering spectrum. An increase in the average dimensions of the nanoparticles in a daguerreotype image would generally have two key optical effects: First, as the horizontal mode becomes more broadband, the image would appear whiter. Second, as the vertical mode shifts outside of the visible range, it would no longer contribute to the optical response of the daguerreotype, thus diminishing the angle-dependent color effect of the image.

We have performed a comprehensive analysis of the plasmonic mechanisms that give rise to the optical response of daguerreotypes using a unique combination of expertise, including nanoscale surface analysis, daguerreotype artistry, and electromagnetic simulations. These early photographs, which can be recast as the first example of plasmonic color printing, can display a wide variety of visual effects that depend on the particular aspects of the plate preparation and exposure processes. However, despite the large range of sizes, morphologies, and even material composition of the nanostructures that are formed on the surface of a daguerreotype, we have identified general features that explain the main characteristics of the optical response of these artworks. In particular, we have found that the nanostructures on the surface support two primary resonances: a transversal dipole mode on the blue side of the spectrum and a vertical dipole mode on the red side. Due to their nature, the first mode radiates predominantly in the vertical direction, while the second one does so at large angles. The interplay between these two behaviors explains the angle-dependent color hue observed in daguerreotypes. Furthermore, we provide a rational explanation for the effect of gilding in the response of the daguerreotype. This process, in which a thin gold layer is added to the plate, results in an overall redshift in the spectra due to the smaller plasma frequency and interband transition threshold of gold compared with silver, but the angle-dependent behavior is maintained. Our results provide a solid background to understand

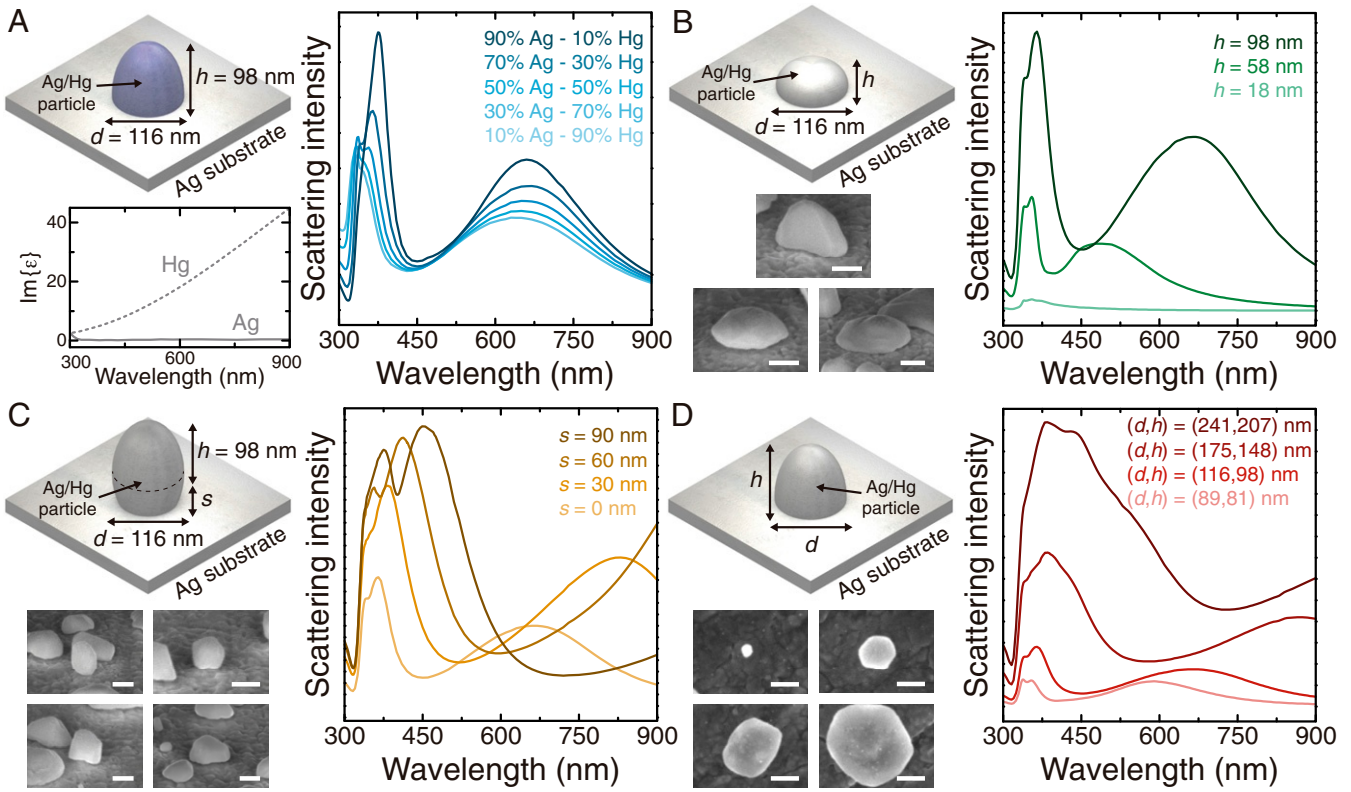

Fig. 4. Effect of particle morphology and composition. (*A*) Scattering intensity for particles with dimensions $d = 116$ nm and $h = 98$ nm (which correspond to the Hg4-UG sample), made of a silver–mercury alloy with different percentages of mercury. *Lower Left Inset* shows the imaginary part of the dielectric function of silver and mercury. (*B*) Scattering intensity for particles with different heights and a fixed diameter, $d = 116$ nm. (*C*) Scattering intensity for particles with fixed dimensions, $d = 116$ nm and $h = 98$ nm, but different levels of penetration into the substrate, *s*. (*D*) Scattering intensity for particles with different diameters, *d*, and heights, *h*. In *B–D*, the material of the nanoparticle is a 70% silver–30% mercury alloy, and *Lower Left Insets* show representative HA-SEM images of the nanostructures on the surface of a daguerreotype. (Scale bars, 200 nm.)

how the optical response of daguerreotypes emerges from the plasmonic properties of the nanoparticles formed on their surface and therefore serve to inform the development of preservation protocols, as well as to provide additional routes and paradigms for advancing plasmonic color printing technology.

Materials and Methods

Daguerreotype Process. The model daguerreotypes for this study were produced by Mike Robinson at Century Darkroom, Toronto, ON, Canada. The protocol to create the model daguerreotype samples was developed to carefully follow 19th-century methods, using modern adaptations only to address safety concerns. First, 0.999 silver (16.5–25.4 μm thickness) was bonded to copper using an industrial rolling mill similar to 19th-century equipment, to create a total plate thickness of 508 ± 25.4 μm. This created a substrate with a silver/copper ratio of 1:19. Polishing abrasive (Nuvite Nushine II S) was applied to the silver surface, which was then polished using a random orbital sander equipped with a 1-inch-thick foam pad covered with a soft cloth disc. The plate was then buffed with iron oxide and lampblack in a linear motion using a 19th-century swing arm holder with velvet paddles. Next, the plate was sensitized using a trisensitization process that alternates iodine and bromine exposure. Iodine and bromine were held in separate Pyrex dishes, intercalated in silica gel. The first iodine exposure was 80 s to yield a yellow/pink tinted surface, followed by the bromine exposure for 80 s to yield a pink/violet surface. Finally, a second iodine exposure for 50 s yielded a magenta-toned surface (48). Using a 19th-century replica camera outfitted with a Voigtländer Petzval lens (serial no. 18922), the plate was given correct exposure ($f/8.5$ for 3 min), followed with a 3× overexposure (stop removed, $f/3.3$ for 3 min) to create solarization around the perimeter using a nonpareil mask (60). The plate was developed with mercury in a fume hood, using an inverted steel pyramid with a small threaded cup containing liquid mercury at the bottom. The plate was placed at the top and the chamber was kept at a constant temperature of 177 °F by a thermocouple. During development, the plate was masked to provide two quadrants with development times of 1 min and 4 min. After development, the plate was immersed in a freshly prepared 3% wt/vol solution of sodium thiosulfate pentahydrate ($Na_2S_2O_3 \cdot 5H_2O$) in distilled water to remove unreacted silver halides and "fix" the image. For the gilded sample, the plate was rinsed after fixing and immediately toned with gold: Using a pipette, 10 drops of 2% sodium metaborate ($NaBO_2 \cdot 4H_2O$) solution were added to 10 mL of a 0.2% gold salt ($HAuCl_4$) solution. This was mixed into 10 mL of a 1% sodium thiosulfate anhydrous ($Na_2S_2O_3$) solution, resulting in an orange-colored solution that turned clear within 2–3 h. The plate was placed on a level support, referred to as a gilding stand, and the gilding solution was pipetted on top. The plate and solution were then heated with an alcohol lamp placed below the stand for 180 s. Finally, the plate was flushed with distilled water and dried with an electric blow dryer. For greater detail and variations, please refer to ref. 48.

Material and Optical Characterization. SEM/HA-SEM and SEM-EDS were performed using a Zeiss Sigma HD VP (10 keV accelerating voltage) equipped with an Oxford Instruments X-Max 80 detector. HA-SEM was done at an angle of 75°–86°, using a 90° angled mount that was back tilted 4°–15°. AFM was performed with a Bruker Dimension in contact mode. Technical photography was accomplished by placing the daguerreotype sample on customized angled mounts and imaging it using a Zeiss Discovery V.12 stereomicroscope equipped with a 45° halogen light source and an Axiocam 506 camera. White balance and light exposures were calibrated at the beginning of each sample set using the grayscale portion of a color calibration card.

Computational Modeling. The numerical calculations of this work were based on the rigorous solution of Maxwell's equations using a commercially available finite-element method solver (COMSOL Multiphysics). In all cases, we considered a single-particle–substrate system, where the particle was partially embedded in the substrate. The particles were modeled as axially

symmetric ellipsoids with the two primary dimensions labeled as *h* and *d*, as shown in Fig. 2*B*. Throughout this work, we analyzed two different types of systems: gilded and ungilded. For the former, unless otherwise specified, the material of the particles was modeled as a mixture of 70% silver and 30% mercury. For the gilded systems, as shown in the schematics of Fig. 3, we added a conformal shell to the particle made of an alloy with 90% gold and 10% silver, with a thickness chosen to match the averaged dimensions of the corresponding experimental samples (≈30 nm). In all cases, the substrate was modeled as a semiinfinite space made of pure silver for the ungilded systems and of an alloy with 90% gold and 10% silver for the gilded ones. This was justified by the fact that the penetration distance of the electric field in gold and silver in the visible range is much smaller than the thicknesses of the substrates of the experimental samples. The dielectric functions of the different materials used in the models were taken from tabulated data. In particular, we used data from ref. 61 for the gold–silver alloy, from ref. 62 for silver, and from ref. 63 for mercury. The dielectric function of the silver–mercury alloy was constructed from the silver and mercury data using the Bruggeman effective medium theory (64). We calculated the optical response for the particle–substrate system using a two-step approach. First, we computed the reflected and transmitted fields from an infinitely extending substrate for a monochromatic plane wave, which had an incidence angle of 45°. In this step, the particle was modeled as a vacuum, and periodic boundaries were used to simulate an infinitely extending domain. The next step used the fields obtained in the previous step as input to calculate the response of the system. The domain size was truncated using perfectly matched layer (PML) domains. These act as near-perfect absorbers, stopping nonphysical reflections from the outer boundaries. Scattering intensities were then calculated by integrating the induced energy flux over a surface, which was selected for either total or angle-dependent scattering. For total scattering, the boundary of integration was the surface of the nanoparticle. For the angle-dependent scattering, we used a semispherical boundary, which collected only light scattered in a 7.5° cone centered on the angle of interest. This two-step simulation was then swept over the range of wavelengths from 300 nm to 900 nm. To simulate the response for unpolarized light, these calculations were done separately for both S and P polarized light, and the final spectra were obtained by averaging the results of these two simulations. When possible, we used symmetry to reduce the computational cost. All of the results presented in the work were checked for convergence with respect to mesh and domain size.

ACKNOWLEDGMENTS. This work has been partially sponsored by the US National Science Foundation (Grant ECCS-1710697). We also acknowledge the University of New Mexico (UNM) Center for Advanced Research Computing for computational resources used in this work. P.G. acknowledges financial support from the UNM Nanoscience and Microsystems program through the Whitten Family Fellowship and the Graduate Assistance in Areas of National Need fellowship. A.E.S. was supported by an Annette de la Renta Fellowship at The Metropolitan Museum of Art (The Met). We are also grateful to our Met colleagues Marco Leona, Department of Scientific Research (DSR); Nora W. Kennedy, Photograph Conservation (PC); and Stephen C. Pinson, Department of Photographs; as well as the City University of New York Advanced Science Research Center and the staff in the Met–DSR, PC, and the Education Departments for their generous support of this project. Photography credits: *Ramesseum, Thebes, 1844*, Joseph-Philibert Girault de Prangey, The Metropolitan Museum of Art. Purchase, Mr. and Mrs. John A. Moran Gift, in memory of Louise Chisholm Moran, Joyce F. Menschel Gift, Joseph Pulitzer Bequest, 2016 Benefit Fund, and Gift of Dr. Mortimer D. Sackler, Theresa Sackler, and Family, 2016 (2016.604).

1. C. E. K. Mees, *From Dry Plates to Ektachrome Film: A Story of Photographic Research* (Ziff-Davis Publishing Company, New York, 1961).
2. C. Löthy, Hockney's secret knowledge, Vanvitelli's camera obscura. *Early Sci. Med.* **10**, 315–339 (2005).
3. E. Ostroff, Ed., *Pioneers of Photography: Their Achievements in Science and Technology* (SPSE, The Society for Imaging Science and Technology, Springfield, VA, 1987).
4. W. Naef, Ed., *Photography: Discovery and Invention: Papers Delivered at a Symposium* (The J. Paul Getty Museum, Malibu, CA, 1990).
5. B. Lavéndrine, J. P. Gandolfo, M. Frizot, S. Monod, *Photographs of the Past: Process and Preservation* (Getty Publications, Los Angeles, CA, 2009).
6. M. S. Barger, W. B. White, *The Daguerreotype: Nineteenth-Century Technology and Modern Science* (Johns Hopkins University Press, Baltimore, MD, 2000).
7. G. Romer, B. Wallis, *Young America: The Daguerreotypes of Southworth & Hawes* (International Center of Photography, George Eastman House, Steidl Publishers, Göttingen, Germany, 2005).
8. L. J. M. Daguerre, Des procédés photogéniques considérés comme moyens de gravure. *C. R. Hebd. Seances Acad. Sci.* **9**, 423 (1839).
9. L. J. M. Daguerre, *An Historical and Descriptive Account of the Various Processes of the Daguerreotype and the Diorama* (McLean & Nutt, London, UK, 1839).
10. R. Taft, *Photography and the American Scene: A Social History, 1839-1889* (Dover Publications, New York, NY, 1964).
11. H. S. Lee, Y. T. Yoon, S. S. Lee, S. H. Kim, K. D. Lee, Color filter based on a subwavelength patterned metal grating. *Opt. Express.* **15**, 15457–15463 (2007).
12. A. C. Arsenault, D. P. Puzzo, I. Manners, G. A. Ozin, Photonic-crystal full-colour displays. *Nat. Photon.* **1**, 468–472 (2007).
13. T. Xu, Y. K. Wu, X. Luo, L. J. Guo, Plasmonic nanoresonators for high-resolution colour filtering and spectral imaging. *Nat. Commun.* **1**, 59 (2010).
14. D. Inoue *et al.*, Polarization independent visible color filter comprising an aluminum film with surface-plasmon enhanced transmission through a subwavelength array of holes. *Appl. Phys. Lett.* **98**, 093113 (2011).
15. S. Kinoshita, S. Yoshioka, J. Miyazaki, Physics of structural colors. *Rep. Prog. Phys.* **71**, 076401 (2008).
16. K. Kumar *et al.*, Printing colour at the optical diffraction limit. *Nat. Nanotechnol.* **7**, 557–561 (2012).
17. Y. Zhao, Z. Xie, H. Gu, C. Zhu, Z. Gu, Bio-inspired variable structural color materials. *Chem. Soc. Rev.* **41**, 3297–3317 (2012).
18. S. J. Tan *et al.*, Plasmonic color palettes for photorealistic printing with aluminum nanostructures. *Nano Lett.* **14**, 4023–4029 (2014).
19. A. S. Roberts, A. Pors, O. Albrektsen, S. I. Bozhevolnyi, Subwavelength plasmonic color printing protected for ambient use. *Nano Lett.* **14**, 783–787 (2014).
20. J. S. Clausen *et al.*, Plasmonic metasurfaces for coloration of plastic consumer products. *Nano Lett.* **14**, 4499–4504 (2014).
21. J. Olson *et al.*, Vivid, full-color aluminum plasmonic pixels. *Proc. Natl. Acad. Sci. U.S.A.* **111**, 14348–14353 (2014).
22. J. Olson *et al.*, High chromaticity aluminum plasmonic pixels for active liquid crystal displays. *ACS Nano* **10**, 1108–1117 (2016).
23. D. Franklin *et al.*, Polarization-independent actively tunable colour generation on imprinted plasmonic surfaces. *Nat. Commun.* **6**, 7337 (2015).
24. T. D. James, P. Mulvaney, A. Roberts, The plasmonic pixel: Large area, wide gamut color reproduction using aluminum nanostructures. *Nano Lett.* **16**, 3817–3823 (2016).
25. R. Yu *et al.*, Structural coloring of glass using dewetted nanoparticles and ultrathin films of metals. *ACS Photon.* **3**, 1194–1201 (2016).
26. L. Shao, X. Zhuo, J. Wang, Advanced plasmonic materials for dynamic color display. *Adv. Mater.* **30**, 1704338 (2018).
27. S. A. Maier, *Plasmonics: Fundamentals and Applications* (Springer, New York, NY, 2007).
28. M. L. Brongersma, Introductory lecture: Nanoplasmonics. *Faraday Discuss.* **178**, 9–36 (2015).
29. T. Xu *et al.*, Structural colors: From plasmonic to carbon nanostructures. *Small* **7**, 3128–3136 (2011).
30. X. Zhu, C. Vannahme, E. Højlund-Nielsen, N. A. Mortensen, A. Kristensen, Plasmonic colour laser printing. *Nat. Nanotechnol.* **11**, 325–329 (2015).
31. A. Kristensen *et al.*, Plasmonic colour generation. *Nat. Rev. Mater.* **2**, 16088 (2016).
32. J. M. Guay *et al.*, Laser-induced plasmonic colours on metals. *Nat. Commun.* **8**, 16095 (2017).
33. I. Freestone, N. Meeks, M. Sax, C. Higgitt, The lycurgus cup - a Roman nanotechnology. *Gold Bull.* **40**:270–277 (2007).
34. P. Colomban, The use of metal nanoparticles to produce yellow, red and iridescent colour, from bronze age to present times in lustre pottery and glass: Solid state chemistry, spectroscopy and nanostructure. *J. Nano Res.* **8**, 109–132 (2009).
35. Y. Zhang *et al.*, Ultrafast light-controlled growth of silver nanoparticles for direct plasmonic color printing. *ACS Nano* **12**, 9913–9921 (2018).
36. A. Swan, C. E. Fiori, K. F. J. Heinrich, Daguerreotypes: A study of the plates and the process. *Scan. Electron Microsc.* **1**, 411–424 (1979).
37. D. L. Hogan *et al.*, Laser ablation mass spectroscopy of nineteenth century daguerreotypes. *Appl. Spectrosc.* **53**, 1161–1168 (1999).
38. V. V. Golovlev, M. J. Gresalfi, J. C. Miller, G. Romer, P. Messier, Laser characterization and cleaning of 19th century daguerreotypes I. *J. Cult. Herit.* **1**, S139–S144 (2000).
39. D. Anglos, K. Melesanaki, V. Zafiropulos, M. J. Gresalfi, J. C. Miller, Laser-induced breakdown spectroscopy for the analysis of 150-year-old daguerreotypes. *Appl. Spectrosc.* **56**, 423–432 (2002).
40. S. A. Centeno, T. Meller, N. Kennedy, M. Wypyski, The daguerreotype surface as a SERS substrate: Characterization of image deterioration in plates from the 19th century studio of Southworth & Hawes. *J. Raman Spectrosc.* **39**, 914–921 (2008).
41. P. Ravines, A. West, J. Minter, R. O. Gutierrez, Jr., "The daguerreotype under high magnification: An ultra-high resolution SEM study of a 19th century daguerreotype's surface nanostructure" in *2nd Latin American Symposium on Physical and Chemical Methods in Archaeology, Art and Cultural Heritage Conservation: Selected Papers. Symposium on Archaeological and Arts Issues in Material Science (LASMAC & IMRC 2009, Cancún, Mexico)*, J. L. Ruvalcaba Sil, J. Reyes Trujeque, J. A. Arenas Alatorre, A. Velázquez Castro, Eds. (Universidad Nacional Autónoma de México, Mexico City, Mexico), pp 99–109.
42. E. Da Silva, M. Robinson, C. Evans, A. Pejović-Milić, D. V. Heyd, Monitoring the photographic process, degradation and restoration of 21st century Daguerreotypes by wavelength-dispersive X-ray fluorescence spectrometry. *J. Anal. At. Spectrom.* **25**, 654–661 (2010).
43. S. A. Centeno, F. Schulte, N. W. Kennedy, A. G. Schrott, The formation of chlorine-induced alterations in daguerreotype image particles: A high resolution SEM-EDS study. *Appl. Phys. A* **105**, 55–63 (2011).

44. E. A. Marquis, Y. Chen, J. Kohanek, Y. Dong, S. A. Centeno, Exposing the sub-surface of historical daguerreotypes and the effects of sulfur-induced corrosion. *Corros. Sci.* **94**, 438–444 (2015).
45. R. Ravines, L. Li, R. McElroy, An electron microscopy study of the image making process of the daguerreotype, the 19th century's first commercially viable photographic process. *J. Imaging Sci. Technol.* **60**, 30504-1–30504-10 (2016).
46. M. S. Kozachuk, T. K. Sham, R. R. Martin, A. J. Nelson, I. Coulthard, Exploring tarnished daguerreotypes with synchrotron light: Xrf and μ-xanes analysis. *Heritage Sci.* **6**, 12 (2018).
47. E. P. Vicenzi, T. Landin, A. A. Herzing, Examination of a 19th century daguerreotype photograph using high resolution scanning transmission electron microscopy for 2D and 3D nanoscale imaging and analysis. *Microsc. Microanal.* **20**, 2000–2001 (2014).
48. M. Robinson, "The techniques and material aesthetics of the daguerreotype," PhD dissertation, De Montfort University, Leicester, UK (2017).
49. S. F. B. Morse, The daguerrotipe. *New-York Observer*, 20 April 1839, 17:16:62.
50. C. Chevalier, Nouvelles instructions sur l'usage du daguerréotype: description d'un nouveau photographe et d'un appareil très simple destiné à la reproduction des épreuves au moyen de la galvanoplastie: suivi d'un mémoire sur l'application du brôme (Chez L'Auteur, Paris, France, 1841).
51. M. A. Gaudin, N. P. Lerebours, *Derniers Perfectionnements Apportés au Daguerréotype* (N.-P. Lerebours, Paris, France, 1842).
52. I. Pobboravsky, *Study of Iodized Daguerreotype Plates* (Information Service, Graphic Arts Research Center, Rochester Institute of Technology, Rochester, NY, 1971).
53. F. Arago, Fixation des images photogéniques sur métal. *C. R. Hebd. Seances Acad. Sci.* **10**, 488 (1840).
54. R. S. Eachus, A. P. Marchetti, A. A. Muenter, The photophysics of silver halide imaging materials. *Annu. Rev. Phys. Chem.* **50**, 11H–144 (1999).
55. S. F. L. Mertens *et al.*, Au@Hg nanoalloy formation through direct amalgamation: Structural, spectroscopic, and computational evidence for slow nanoscale diffusion. *Adv. Funct. Mater.* **21**, 3259–3267 (2011).
56. I. Brodie, M. Thackray, Photocharging of thin films of silver iodide and its relevance to the Daguerre photographic process. *Nature* **312**, 744–746 (1984).
57. E. González, J. Arbiol, V. F. Puntes, Carving at the nanoscale: Sequential galvanic exchange and Kirkendall growth at room temperature. *Science* **334**, 1377–1380 (2011).
58. S. A. Centeno, N. W. Kennedy, G. B. Romer, A. E. Schlather, A. Cervera Xicotencatl, "Un daguerréotype monstre" in *Monumental Journey: The Daguerreotypes of Girault de Prangey*, S. C. Pinson *et al.*, Eds. (Metropolitan Museum of Art, New York, NY, 2019).
59. A. Sobhani *et al.*, Pronounced linewidth narrowing of an aluminum nanoparticle plasmon resonance by interaction with an aluminum metallic film. *Nano Lett.* **15**, 6946–6951 (2015).
60. W. Yarnall, "Improvement in daguerreotyping." US Patent 9511A (1852).
61. D. Rioux *et al.*, An analytic model for the dielectric function of Au, Ag, and their alloys. *Adv. Opt. Mater.* **2**, 176–182 (2014).
62. P. B. Johnson, R. W. Christy, Optical constants of the noble metals. *Phys. Rev. B* **6**, 4370–4379 (1972).
63. T. Inagaki, E. T. Arakawa, M. W. Williams, Optical properties of liquid mercury. *Phys. Rev. B* **23**, 5246–5262 (1981).
64. D. E. Aspnes, Local-field effects and effective-medium theory: A microscopic perspective. *Am. J. Phys.* **50**, 704–709 (1982).